Int J Adv Manuf Technol (2016) 85:1035–1044
DOI 10.1007/s00170-015-7974-5

ORIGINAL ARTICLE

Surface tension-powered build dimension control in laser additive manufacturing process

Y. S. Lee[1] · D. F. Farson[1]

Received: 16 July 2015 / Accepted: 12 October 2015 / Published online: 31 October 2015

Abstract This research is aimed at providing insight into the process phenomena that determine the surface finish quality and dimensional accuracy of laser additive manufactured parts. It was found that melt pool fluid flow has a major effect on the sidewall dimensions of the final deposit. Thermocapillary gradient is the main driving force for melt pool flow, and the gradient can potentially be controlled by material composition. Thus, the effects of three characteristic thermocapillary gradients (positive, negative, mixed) on melt pool fluid flows and build geometry are investigated in this study. The work studied mechanisms responsible for sidewall nonuniformity and deposit bulge in detail. The results showed that the bulge in deposit width occurring at the start of the build is reduced by approximately 56 % by deposition of material having mixed thermocapillary gradient as compared to the bulge resulting from deposition of material with a negative thermocapillary gradient. Also, melt pool temperature distributions are visualized during laser deposition of five-layer single-track builds. More accurate build geometry and reduced deposit sidewall bulge can be expected to lead to lower total cost of additive manufactured parts.

Keywords Laser additive manufacturing · Melt pool fluid flow · Transport simulation · Thermocapillary gradient · Surface finish · Deposit bulge

✉ D. F. Farson
farson.4@osu.edu

[1] Department of Materials Science and Engineering, Welding Engineering Program, The Ohio State University, Columbus, OH 43221, USA

1 Introduction

Laser additive manufacturing (LAM) is considered to be an important new commercial manufacturing technology, and there has been considerable research to understand the process and to prove and refine its capabilities. LAM has huge potential for near net shape fabrication of highly complex parts but also creation of graded structures by simultaneous deposition of dissimilar metal powders [1, 2]. Despite these unique advantages, broad application of LAM has been impeded by issues with cost and production rate and the difficulty of predicting the dimensional tolerances and properties of finished products. Overcoming these issues requires deep understanding of the relationships between process parameters, melt pool fluid flow and geometry, and predicted melt pool shape and build microstructure from a numerical simulation of the LAM process [2, 3].

LAM is a layer-by-layer deposition process that uses simultaneous metal powder injection and laser heat input to form a melt pool on top of previously deposited material. A schematic illustration of blown powder LAM process is shown in Fig. 1. The powder particles are carried by an inert gas through the annular powder feed nozzle surrounding a concentric focused laser beam. The laser heat input melts the powder particles and the surface of the previously deposited layer to form a melt pool, which is traversed linearly and solidifies to form a deposit layer. Only the powder particles hitting the melt pool contribute to formation of deposit layer. Others ricochet from the substrate solid surface. The flowing powder particles create a powder cloud between the nozzle exit and substrate. The laser beam interacts with and heats the particles in the cloud, and the laser power is attenuated by absorption, reflection, and radiation due to the laser–powder interactions [4]. Numerical simulation in predicting the individual particle motions and laser–powder interactions is too computationally intensive to

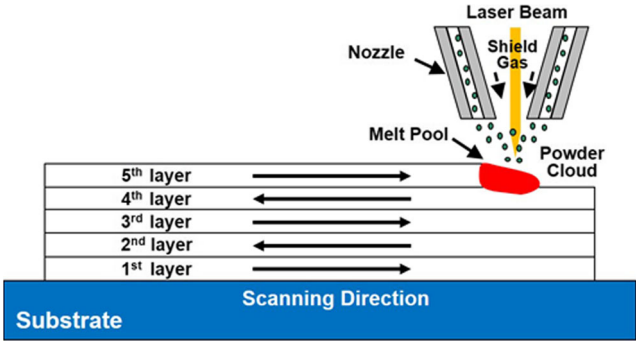

Fig. 1 Illustration of laser additive manufacturing process and deposit sequence

be practical. More recently, researchers have performed experiments to measure overall laser absorption, reflection, transmission, and thermal radiation due to laser–powder cloud interactions for known deposition process parameters [5].

Prior researchers have developed numerical laser cladding simulations that quantitatively predict specific aspects of heat flow or melt pool phenomena relevant to laser additive manufacturing [6–12]. However, fluid flow simulations for LAM are still at an initial stage of development [13] since laser–powder–substrate interactions are complex, and accurate representation of process parameter interactions is challenging. As a result, a relatively small number of LAM simulations have been reported. Most prior studies utilized finite element method (FEM) [10, 14, 15], which does not explicitly calculate heat convection by melt pool fluid flow. Prior transport fluid simulations investigated multiple layer builds with a predefined melt pool surface shape [13] and two or three layers [16, 17]. Therefore, a more advanced melt pool transport simulation of the LAM process will help to not only understand the relationship between melt pool shape and process parameters but also identify process modifications that improve surface finish quality.

Although laser additive manufactured parts typically are used with little or no post machining, dimensional accuracy of as-deposited parts may still not be sufficient for applications requiring high precision parts. Moreover, post-process machining may not be possible for internal features or complex external geometries. Ideally, optimum surface finish and dimensional accuracy would be obtained if deposition were done with a thin and stable deposit melt pool that is invariant with process parameters and fluid dynamics. However, in reality, melt pool shape changes with various fluid forces (thermocapillary stress and buoyancy force) and external process inputs (momentum force by injected powder particles and shield gas pressure) applied to the melt pool [3, 18]. For instance, thermocapillary-driven fluid flow, often called Marangoni flow or thermocapillary convection, strongly influences melt pool shape, heat, and mass transfer that eventually change temperature gradient, surface finish, and dimension accuracy of laser additive manufactured parts.

The spatial variation of thermocapillary due to surface temperature variation of the melt pool always causes molten metal to flow from lower to higher surface tension regions. Yet, since thermocapillary is temperature- and composition-dependent, the thermocapillary gradient can be changed from negative to positive and vice versa [19] by changing these variables. The relationship between thermocapillary gradient, temperature, fluid flow pattern, and resulting melt pool shapes is illustrated in Fig. 2. For an axisymmetric melt pool with a negative thermocapillary gradient, thermocapillary stress radially carries fluid outward from the center shown in Fig. 2a. As a result, the melt pool has wide and shallow shape. For the melt pool with a positive thermocapillary gradient illustrated

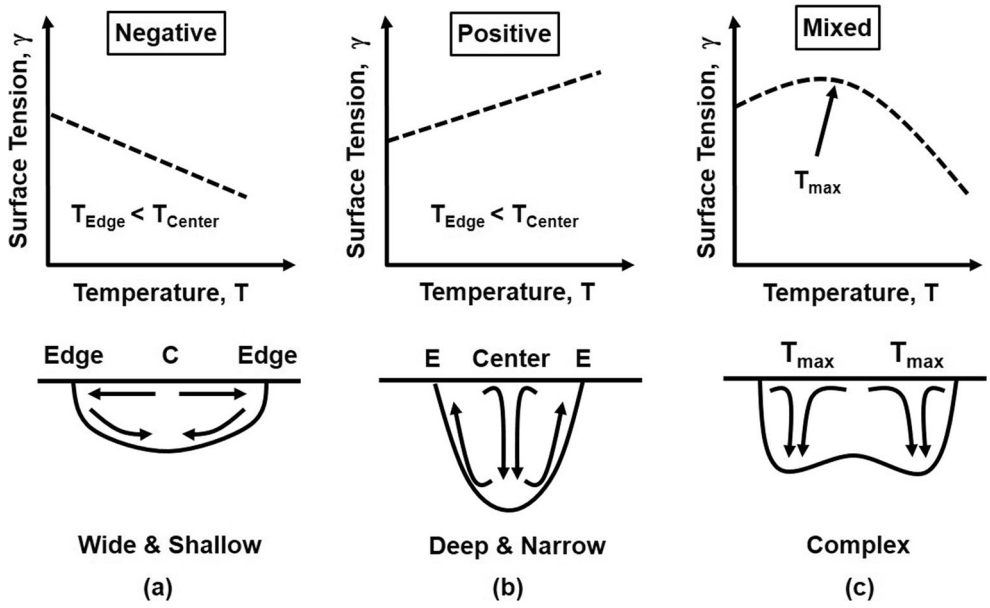

Fig. 2 Different fluid flow pattern and melt pool shapes produced by different directions of thermocapillary gradient: **a** negative, **b** positive, and **c** mixed gradient

in Fig. 2b, the fluid flow becomes reversed from radially outward to radially inward, and the melt pool shape is altered to narrow and deep. In the illustration for a mixed thermocapillary gradient in Fig. 2c, two opposing fluid flows collide, and the shape of the weld pool bottom becomes nonuniform. A mixed gradient is produced in the melt pools containing parts per million levels of sulfur. The change in thermocapillary temperature gradient from positive to negative is found at the maximum point corresponding to temperature $T_{\max}$. The location of this maximum temperature varies with the concentration of surface active elements (for example, sulfur or oxygen) on the melt pool surface. The latter is interesting for applications because oxygen content in the LAM build chamber atmosphere can be accurately controlled.

In the present research, the melt pool transport simulation is used to investigate the effect of thermocapillary–temperature gradient on melt pool fluid flow pattern. Moreover, the melt pools with mixed thermocapillary gradients having varying $T_{\max}$ are simulated to predict the resulting changes of melt pool shape and build deposit geometry. This research aids in the selection of thermocapillary–temperature gradient for the best build surface finish quality and also provides insights into underlying fundamentals of the LAM process.

2 Physical model

2.1 Governing equations

LAM process always involves complex physical phenomena associated with continuous powder injection and laser heating of the molten pool. The addition of mass, energy, and momentum alters fluid temperature and flow resulting in change of weld pool size and shape. Thus, transient analysis of transport phenomena in and around the melt pool as material is deposited is essential. In this study, numerical simulation (Flow3D, FlowScience) is used to predict melt pool transport phenomena based on conservation equations of mass, energy, and momentum. The transport expressions used in the simulation are given as:

$$\frac{\partial \rho}{\partial t} + \nabla \cdot \left(\rho \vec{v}\right) = \dot{m}_s \tag{1}$$

$$\frac{\partial h}{\partial t} + \left(\vec{v} \cdot \nabla\right) h = \frac{1}{\rho}(\nabla \cdot \kappa \nabla T) + \frac{\dot{h}_s}{\rho} \tag{2}$$

$$\frac{D\vec{v}}{Dt} = -\frac{1}{\kappa}\nabla P + \mu \nabla^2 \vec{v} + \vec{g}[1-\beta(T-T_m)] + \frac{\vec{p}_s}{\kappa} \tag{3}$$

Incompressible and Newtonian fluid are assumed. Here, ρ is density of liquid metal, t is time, $\vec{v}$ is fluid velocity vector, $\dot{m}_s$ is mass addition rate, h is enthalpy, κ is thermal conductivity, T is temperature, $\dot{h}_s$ is rate of enthalpy addition associated with the added material, P is hydrodynamic pressure, μ is viscosity, $\vec{g}$ is gravitational acceleration vector in z direction, β is thermal expansion constant, T_m is melting temperature, and $\dot{\vec{p}}_s$ is momentum addition rate associated with the mass addition.

The simulation uses the volume of fluid (VOF) method to predict the transient location and shape of the void–fluid interface by simultaneously solving the above conservation equations with a fourth equation representing conservation of volume expressed as:

$$\frac{\partial F}{\partial t} + \nabla \cdot \left(\vec{v} F\right) = \dot{F}_s \tag{4}$$

where F denotes fluid volume fraction in a simulation grid cell, and $\dot{F}_s$ is a change in F associated with fluid density and mass source rate. F=0 indicates a void region where no fluid is present, and F=1 indicates completely filled fluid region. An intermediate value of $0<F<1$ indicates that a cell contains an interface between void and fluid regions. Metal powder and laser heat inputs to the melt pool are represented by source terms in all of above conservation equations.

2.2 Boundary conditions and physical properties

For a reasonably accurate simulation, several calibrations were made to process inputs. To approximate laser heating in the LAM process, laser–powder–substrate interaction should be considered. Laser energy input to the melt pool is decreased by reflection, radiation, and absorption by powder particles and by reflection, convection, and radiation from the melt pool surface. Values for these energy losses have been reported in prior experimental literature [5]. Nine percent loss was measured for absorption and reflection from the powder cloud and 1 % for convection and radiation from the substrate. Laser reflectance varies significantly with deposit geometry, substrate material, surface oxidation, beam incident angle, and laser polarization and wavelength, an approximate value of 50 % reflectance (40 % absorptance) at the pool surface was assumed for this study. For comparison, the Hagen–Rubens relationship [20] was used for Nd–YAG laser wavelength and predicts absorptance of 35 % at 1533 K (solidus) and 43 % at 1609 K (liquidus). Thus, the absorptance of 40 % used in this simulation is reasonable.

A moving laser with flat top distribution [21] was used as a surface heat flux boundary condition in the simulation. The heat flux equation for flat top distribution is given as:

$$q(r) = \frac{Q}{\pi r^2} \tag{5}$$

where q is heat flux at the surface, Q is magnitude of heat input, and r is laser beam spot size in radius. The heat is conducted and convected in the melt pool and build deposit.

A mass flux for the powder injection was incorporated into the computation domain just above the free surface of the substrate. The position of the source was elevated as the layers were deposited. The initial temperature of powder particles injected into the melt pool was assumed to be just above the liquidus temperature.

The powder catchment efficiency can be estimated by the ratio between total powder input and amount of powder contributing to formation of the deposit layer. A value of 47 % was assumed as reasonable based on the work of Weisheit et al. [22].

As described previously in discussion of Fig. 2, thermocapillary gradient is well known to be a significant driving force for flow in conduction mode laser melt pools that has significant effects on fluid circulation and resulting pool shape. Three different types of thermocapillary–temperature gradients are used in the present study: negative, positive, and mixed are shown in Fig. 3 below. All three types (in four cases) have a surface tension of 1842 dyne/cm at the liquidus temperature, taken from experimental data for the surface tension of pure alloy IN718 [23].The negative type corresponds to a thermocapillary gradient coefficient of −0.11 dyne/cm K at temperatures above the liquidus. However, the presence of surface active elements such as sulfur or oxygen can cause positive thermocapillary gradients at temperatures above the liquidus temperature. In this simulation, the positive thermocapillary used a gradient coefficient of +0.11, opposite to the negative gradient. The mixed gradient is the most realistic for fluids containing surface active elements [24, 25]. The mixed thermocapillary gradient–temperature relationship depends on sulfur content of the material. Sulfur concentrations of 6 and 10 ppm are assumed in this study. The temperatures at which the peak of thermocapillary occurs are 1818 and 1941 K, respectively. More details of the mixed thermocapillary–temperature calculation have been given in a previous publication [4].

The simulation was conducted in a 3D computation domain with dimensions of 2.8 cm (X-direction), 1.5 cm (Y-direction), and 0.9 cm (Z-direction) as shown in Fig. 4 below. The substrate occupies the region $0<Z<0.5$ cm, and void occupies the region $0.5<Z<0.9$. The region $0<Z<0.4$ is meshed with coarse mesh blocks to reduce computational load. The upper fine mesh block has 262,500 cubic cells with edge length of 200 μm, and the lower block contains coarse mesh block 26,600 cubic cells with edge length of 400 μm.

Thermophysical properties and manufacturing parameters used in this simulation are given in Table 1. The powder particles and substrate material are both Ni-based superalloy IN718. The room temperature is assumed as 300 K for material and surroundings.

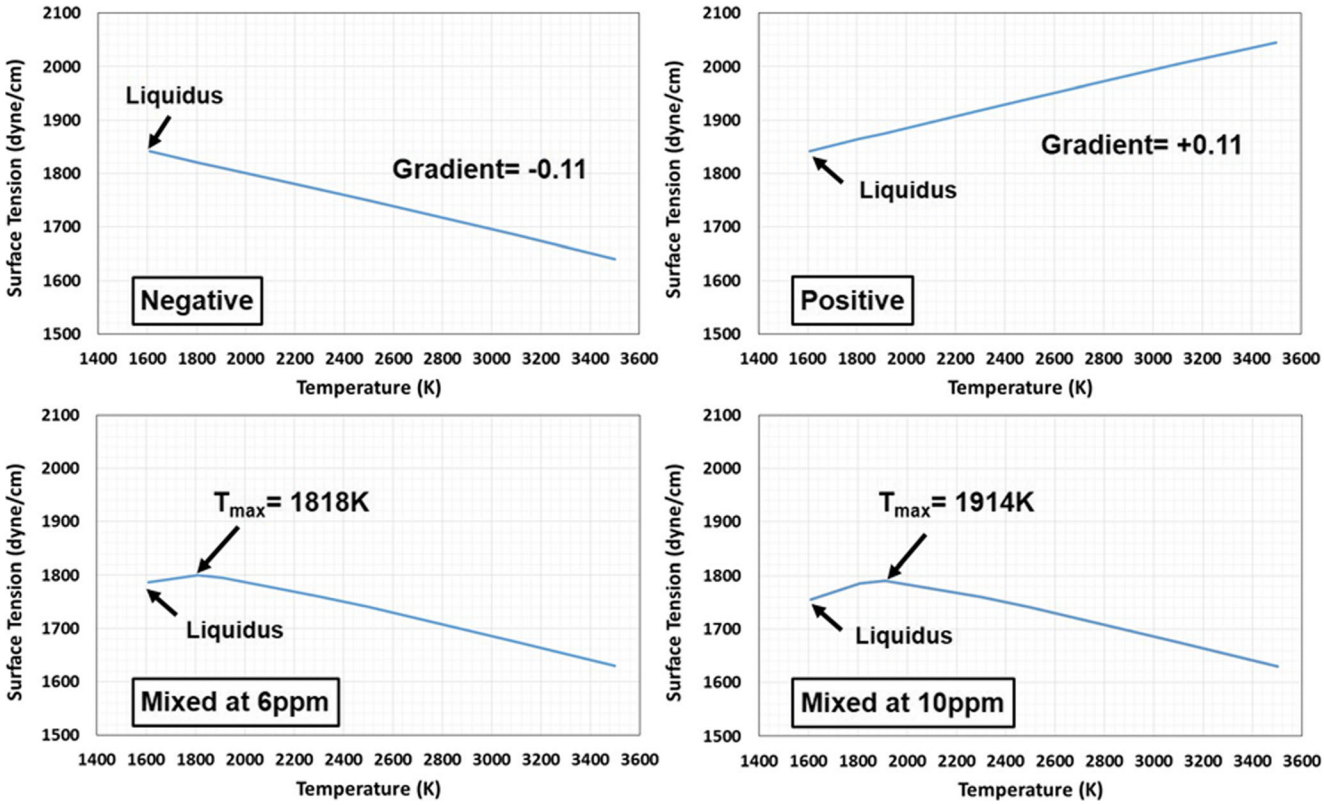

Fig. 3 Surface tension–temperature gradients used in the simulations: negative, positive, and mixed at 6 and 10 ppm sulfur

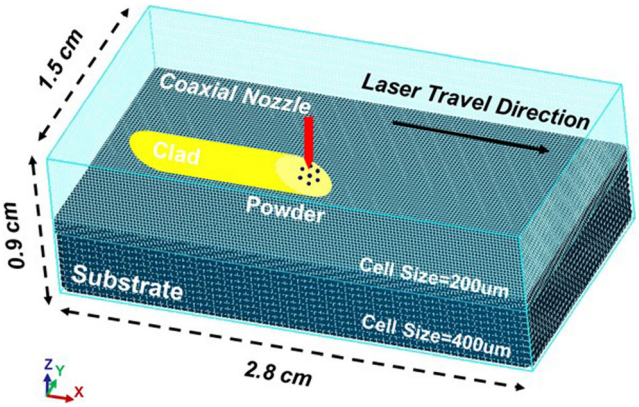

Fig. 4 Schematic description of computation domain

3 Result and discussion

Simulation predictions of additive manufacturing deposit dimensions and temperatures are comparable to experimental measurements reported in literature [26]. In comparison with the literature, the prediction errors for peak temperature at mid-center of the deposit were less than 2.5 % for all deposit layers, and prediction errors for deposit mid-center height and width were in the range 11.5–11.9 %.

A characteristic build deposit feature referred to as a bulge can be seen in Figs. 5 and 6. The cause of the bulge has been previously studied in laser and hybrid laser–arc welding. It was reported that the bulge is usually observed at the starting point of the deposit and is related to fluid flow to minimize surface tension of the deposit [28, 29]. Also, it was found that longer melt pools can lead to larger bulge widths because the longer pool allows more molten metal to flow to the rear of the melt pool in response to thermocapillary force. Morgan et al. [30] addressed the roles of surface tension force and energy minimization in producing spherical melt pool free surfaces. Asymmetric downward bulging of deposits on a vertical surface was shown during the laser rapid manufacturing process [31]. It noted that gravity is the key factor causing the downward rounded bulge. Based on prior literature, understanding of interactions between surface tension, gravity, and fluid convection is essential to explain the bulging mechanisms in LAM.

Table 1 Thermophysical properties and manufacturing parameters used in simulation

Property and parameters	Value [units]
Specific heat of liquid	7.25e+06 [cm^2/s^2 K]
Specific heat of solid	5.77e+06 [cm^2/s^2 K]
Conductivity of liquid	2.928e+06 [g cm/s^3 K]
Conductivity of solid	2.792e+06 [g cm/s^3 K)
Liquidus temperature	1609 [K]
Solidus temperature	1533 [K]
Latent heat	2.27e+09 [cm^2/s^2]
Viscosity	0.196*exp(5848/T) [mPa]
Density of liquid	[7400–0.88 (T-1609)]/1000 [g/cm^3]
Density of solid	[8190–0.392 (T-298)]/1000 [g/cm^3]
Surface tension	1842 [dyne/cm]
Thermocapillary gradient coefficient	+−0.11 [dyne/cm K]
Beam spot size	1.95 [mm]
Powder feed rate	7 [g/min]
Beam power	700 [W]
Idle time between passes	Continuous [s]
Powder catchment efficiency	47 [%]
Velocity of laser beam	1.083 [cm/s]

Source: [22, 23, 26, 27]

The effect of thermocapillary gradient on deposit sidewall geometry can be understood by analysis of the simulation results shown in Fig. 5. Five layer deposits created with melt pools having negative and positive thermocapillary gradient are displayed in Fig. 5a, b, respectively. In both cases, the distinctive bulge of the deposit sidewall is observed at starting position. For simulations with melt pools having mixed thermocapillary gradient with maximum temperatures T_{max} of 1818 K and 1914 K in Fig. 5c, d, a decrease in the width of the sidewall bulge is noted for both mixed thermocapillary gradients. The variation of bulge width with thermocapillary gradient types is illustrated by the cross sections in Fig. 6. These results are studied in more detail to better understand the effects of thermocapillary gradient on deposit dimensions in Figs. 7, 8, and 9.

The effect of the bulge on deposit sidewall dimension can be expressed in a simple subtraction of minimum width from maximum width. Image processing software (ImageJ, NIH) is used to measure the maximum and minimum values from the simulated results shown in Fig. 6. The deposit manufactured with material having the negative gradient type, shown in Fig. 6a, has the largest bulge width of 475 μm. A deposit made with material having positive thermocapillary gradient is shown in Fig. 6b. The bulge width is decreased by approximately 100 μm compared to the negative gradient case. In Fig. 6c, d, further reduction in the bulge width is observed for the mixed thermocapillary gradients with two different levels of sulfur. The value is 272 μm for 6 ppm and 208 μm for 10 ppm. It is noted that bulge width is decreased by approximately 56 % compared to that for the negative gradient. From these results, it is concluded that nonuniform and inhomogeneous surface finish can be optimized by manipulating thermocapillary gradient.

Figure 7 displays the bulge and the fluid flow pattern in the melt pool at fifth layer deposit with a negative thermocapillary gradient. The deposit is cross-sectioned along A–A line

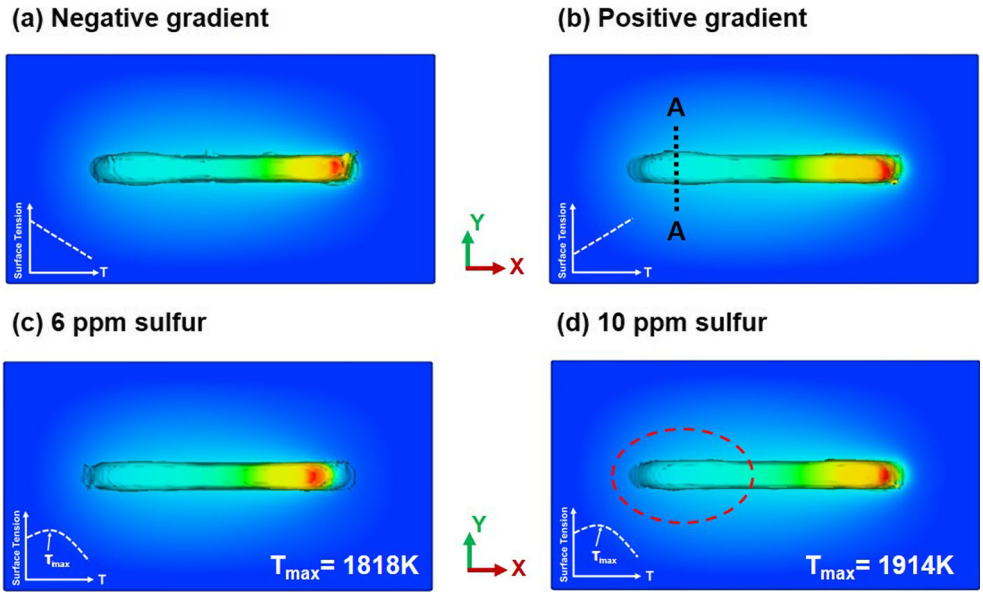

Fig. 5 Effect of thermocapillary gradients on deposit geometry at the starting position

shown in Fig. 5b. The bulge is not observed on the sidewall of deposit in Fig. 7a. Mainly outward fluid flow along the melt pool surface exists, and the surface fluid velocity is the fastest in the melt pool. In Fig. 7b, downward flow begins to develop at the melt pool edge, and the velocity decreases to 8.51 cm/s. At this step, the bulge starts to form at the edges but it is not large. In Fig. 7c, d, the bulge becomes more pronounced at the edges with the increase of the width and height of the melt pool and the fluid velocity. In Fig. 7e–h, the bulging action is dominant and enhances a peculiar convex melt pool bottom shape at fusion boundary. As the returning flow develops along the bottom edge of the melt pool, the flow pushes the fusion boundary of the pool inward at the edges. Consequently, the pool has a more obtuse angle at outer edge. As the beam moves away, the pool cools and solidifies. Thus, the pool bottom moves upward, and the fluid velocity becomes slower and slower.

The bulge in multiple-layer additive manufacturing is much more complex phenomena than that in conventional welding or one-layer laser additive manufacturing process because it is caused by interaction of surface tension, gravity effect associated with interaction time between deposit layers, and fluid convection. First, surface tension tends to make a generally round melt pool surface shape to minimize surface energy. However, the deposit shape at the edges is not perfectly round due to gravity effect. Also, interaction time between the fourth and fifth deposition layers has important effects on melt pool size, shape, and fluid flow at times near the beginning of the fifth layer. The top solid surface of the fourth layer is at a relatively high temperature at the start of the fifth deposition layer because heat input at the end of the fourth layer has not had much time to dissipate due to continuous deposition process. Therefore, the melt pool fluid volume becomes larger and deeper, and the average temperature increases. As a result of the increased temperature, viscosity and density of the fluid decrease so that the melt pool has less resistance against gravity force. The melt pool size and gravity force at the bottom of the melt pool are larger, and there is more

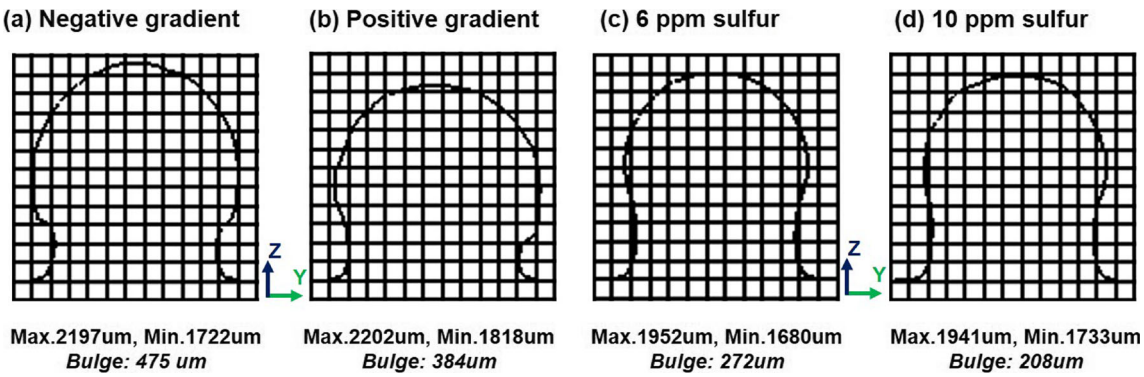

Fig. 6 Measurement of simulated deposit widths and their variance with thermocapillary gradients. A cell size is 200 μm

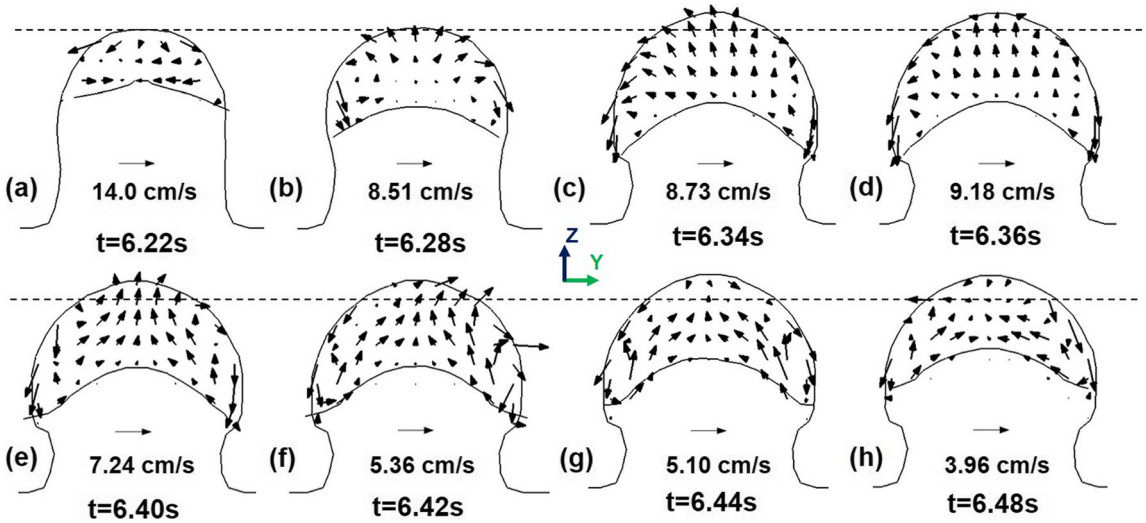

Fig. 7 Evolution of a bulge at the edges of the deposit near the start of deposition in the fifth layer of material with a negative thermocapillary gradient

tendency for the melt to slide down the edge of the deposit. Lastly, outward surface fluid flow due to the negative thermocapillary gradient pushes the liquid to the edges so that the sidewall of the deposit expands. Meanwhile, the combined force of downward flow and gravity pushes the fluid down along the surface of the sidewall. As a result, the sidewall has the bulged edges.

Figure 8 illustrates the evolution of fluid flows and the sidewall of the deposit at a time near the beginning of deposition of the fifth layer with fluid having positive thermocapillary gradient. In Fig. 8a, there is no bulge observed at the sidewall of the deposit. In Fig. 8b, the inward and downward fluid flow begins to develop at the top center of the melt pool surface due to the positive thermocapillary gradient. As a result, a concave melt pool bottom is created at the fusion boundary. As the melt pool size increases due to remelting of the fourth layer and deposition of additional material, the maximum fluid circulation velocity increases to 17.4 cm/s in Fig. 8c. In Fig. 8d, a slight amount of sidewall bulging can be noted. In Fig. 8g, the bulge has become more pronounced, and the maximum fluid velocity on the pool surface has decreased to 8.83 cm/s. In Fig. 8h, there is inward and downward flow at the center of the melt pool. Interestingly, although the simulation predicts similar bulge sidewall shapes in deposits made with melt pools having negative and positive gradients, the fluid flow patterns that form the bulge are significantly different.

Figure 9 shows the fluid flow in the melt pool and transient evolution of the deposit made with material with 10 ppm sulfur and a mixed thermocapillary gradient. At the beginning of the fifth layer deposition in Fig. 9a, the dominant flow pattern is outward and downward so the tendency to bulging at the sideway is strong. However, in Fig. 9b–g, collision of two opposing flows caused by the transition of the thermocapillary

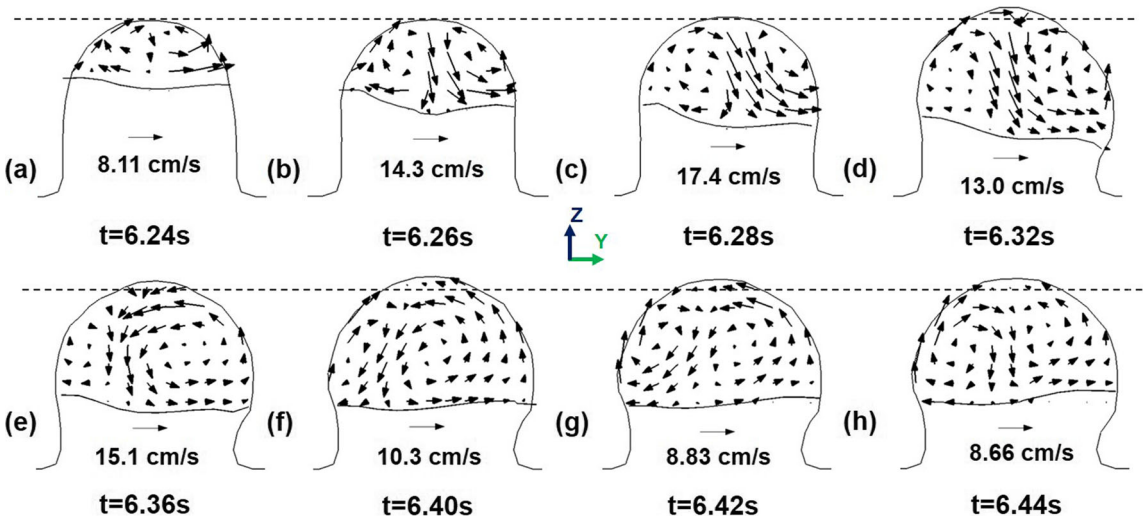

Fig. 8 Evolution of fluid flow and bulging of weld deposit side at the start of the fifth layer of deposition of material with a positive thermocapillary gradient

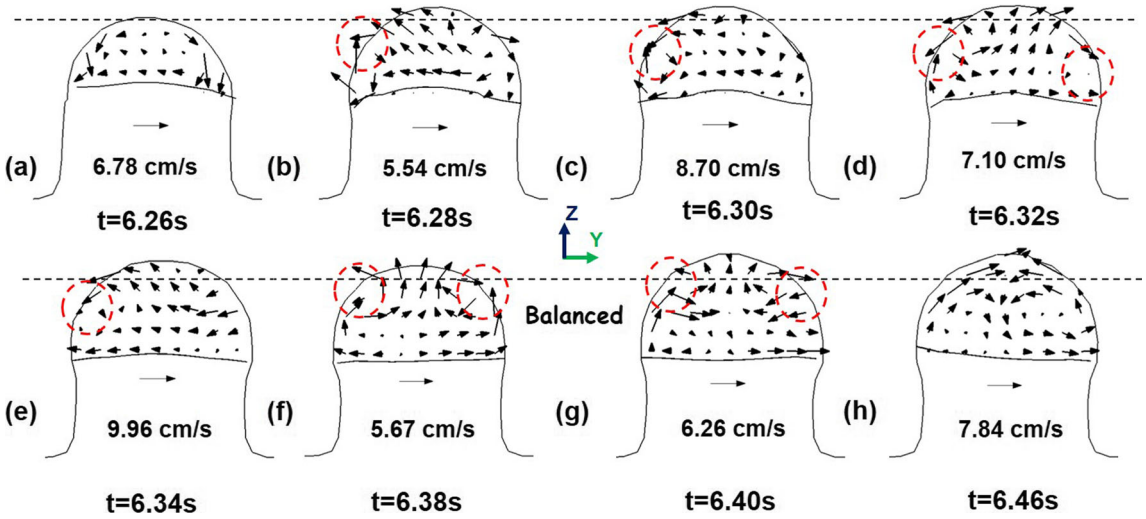

Fig. 9 Evolution of fluid flow and bulging of weld deposit side during fifth layer deposition in mixed thermocapillary gradient (10 ppm sulfur case)

gradient is observed. The region of colliding flows is highlighted by a red dashed circle. Once collision of opposing surface flows occurs, the resultant downward flow is produced at the mid area of the melt pool. Unlike the purely positive and negative thermocapillary gradient cases, this downward flow appears to reduce the bulging action in this case of mixed thermocapillary gradient with 10 ppm sulfur.

Figure 10 shows temperature distributions in X–Y horizontal sections of deposits made with fluids having different thermocapillary gradients. The time is 6.40 s, near the beginning of deposition of the fifth layer (the cooler blue-colored material at the right of the figures is the unmelted top surface of the fourth layer). The z-axis location of the section is at the location of the maximum bulge width, which is somewhat above the bottom of the fifth layer melt pool. Those are taken from simulations with melt pools having negative, positive, and mixed 10 ppm sulfur gradients. The maximum temperature is observed at the edge of deposit in Fig. 10a, whereas the maximum temperature is located in the center region in Fig. 10b. Unlike the prior two cases, a relatively uniform distribution is observed in the melt pool for the mixed gradient case shown in Fig. 10c. The cause of the different temperature distribution can be explained by the fluid flow patterns as discussed above. With materials with negative thermocapillary gradient in Fig. 10a, hot molten fluid is first pushed out to the edge at the top surface of the deposit and slides downward. Thus, it undergoes additional convectional cooling by shielding gas. As a result, a lower maximum temperature of 1716 K is found in the negative gradient case. In contrast, for material with positive thermocapillary gradient in Fig. 10b, flow carries the hot molten fluid to the center first so that inward and downward flow keeps higher temperature inside at the center of the deposit. There is less convectional cooling made by the surrounding gas. Thus, the fluid can remain at a relatively high maximum temperature of 1885 K compared to the negative gradient case. In Fig. 10c, the maximum temperature is the lowest at 1606 K, and temperature distribution is relatively uniform along Y direction because collision of opposing hot and cold fluid flow mixes leads to additional reduction of maximum temperature and temperature gradient throughout the cross section. Because maximum temperature, temperature distribution, and its gradient are different at the three thermocapillary gradient cases, it can be assumed that different scales of solidified microstructures will be produced at the sides and center of the deposit due to variation of temperature gradient and solidification rate at

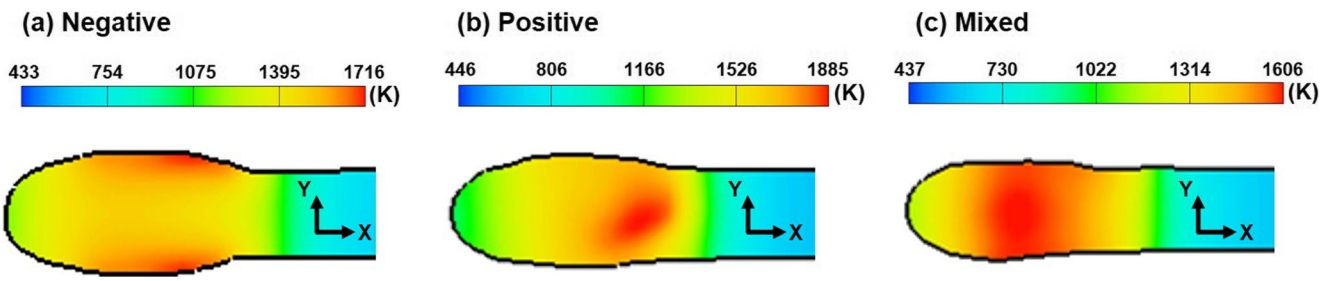

Fig. 10 Characteristic temperature distributions near the beginning of the fifth layer in deposits made with material having melt pools with **a** negative, **b** positive, and **c** mixed thermocapillary gradients

the melt pool solidification boundary. Efforts to predict microstructure variation in LAM deposits using the 3D transport simulation are planned in the future.

4 Summary and conclusion

The numerical simulation developed by this work provided insight into distinct melt pool fluid flow patterns occurring during laser additive manufacturing with material compositions that result in three different types of thermocapillary gradients and their effect on the final build geometry. The simulation results showed that bulge at the start of the build was reduced by melt pool having a mixed thermocapillary gradient. The lateral width of the bulge was approximately 56 % less than that of the bulge width of a deposit made with a material having a negative gradient. Thus, it can be said that nonuniformity and surface finish of the deposit sidewall can be optimized by the manipulation of the thermocapillary gradient of the melt pool present during layer-by-layer deposition. More accurate build geometry and reduced sidewall bulge can be expected to lead to lower cost of flexible manufactured parts. Also, the simulation results showed effects of the particular fluid flow patterns for the various thermocapillary gradient types on deposit and build geometry. Interestingly, a similar mushroom-shaped bulge was produced at the lateral edge of the start of deposits made with material having both positive and negative gradients. In comparison, the collision of opposing melt pool fluid flows that occurred during deposition of material having mixed gradient minimized deposit bulging. Characteristic build temperature distributions in X–Y cross sections were predicted for deposition with the three different thermocapillary gradients. Different thermocapillary gradients led to different maximum temperature, temperature distribution, and solidification gradient and rates which would result in different solidified microstructure and properties of the build. Further research is required to define the relationships between solidification conditions and final microstructure and properties of the multilayered deposit. Also, further experimental efforts are planned for direct comparison of simulated and experimental deposit cross sections. Overall, this work contributes to application of melt pool simulation for LAM process as well as suggestion of a possible method for reduction of manufacturing cost based on the understanding of the relationship between thermocapillary gradient, fluid flow motion, and resultant change of melt pool and deposit geometry.

Acknowledgments The authors would like to thank Center for Integrative Materials Joining Science for Energy Applications (CIMJSEA), Award No. 134729, for supporting this project. The authors also express their thanks to Prof. W. Zhang for their helpful support and interest in this project.

References

1. Zhou JH, Zhang YW, Chen JK (2009) Numerical simulation of random packing of spherical particles for powder-based additive manufacturing. J Manuf Sci Eng 131(3):031004
2. Mazumder J, Schifferer A, Choi J (1999) Direct materials deposition: designed macro and microstructure. Mater Res Innov 3(3): 118–131
3. Gharbi M, Peyre P, Gorny C, Carin M, Morville S, Le Masson P, Carron D, Fabbro R (2013) Influence of various process conditions on surface finishes induced by the direct metal deposition laser technique on a Ti-6Al-4V alloy. J Mater Process Technol 213(5): 791–800
4. Lee YS, Nordin M, Babu SS, Farson DF (2014) Influence of fluid convection on weld pool formation in laser cladding. Weld J 93(8): 292S–300S
5. Gedda H, Powell J, Wahlstrom G, Li WB, Engstrom H, Magnusson C (2002) Energy redistribution during CO_2 laser cladding. J Laser Appl 14(2):78–82
6. Tabernero I, Lamikiz A, Ukar E, Martinez S, Celaya A (2014) Modeling of the geometry built-up by coaxial laser material deposition process. Int J Adv Manuf Technol 70(5–8):843–851
7. Wen SY, Shin YC (2010) Modeling of transport phenomena during the coaxial laser direct deposition process. J Appl Phys 108(4): 044908
8. Vasquez F, Ramos-Grez JA, Walczak M (2012) Multiphysics simulation of laser-material interaction during laser powder deposition. Int J Adv Manuf Technol 59(9–12):1037–1045
9. Choi J, Han L, Hua Y (2005) Modeling and experiments of laser cladding with droplet injection. J Heat Transf 127(9):978–986
10. Toyserkani E, Khajepour A, Corbin S (2004) 3-D finite element modeling of laser cladding by powder injection: effects of laser pulse shaping on the process. Opt Lasers Eng 41(6):849–867
11. Picasso M, Rappaz M (1994) Laser-powder-material interactions in the laser cladding process. J Phys IV 4(C4):27–33
12. Balu P, Hamid S, Kovacevic R (2013) Finite element modeling of heat transfer in single and multilayered deposits of Ni-WC produced by the laser-based powder deposition process. Int J Adv Manuf Technol 68(1–4):85–98
13. Manvatkar V, De A, DebRoy T (2014) Heat transfer and material flow during laser assisted multi-layer additive manufacturing. J Appl Phys 116(12):124905
14. Kumar A, Paul CP, Padiyar AS, Bhargava P, Mundra G, Kukreja LM (2014) Numerical simulation of laser rapid manufacturing of multi-layer thin wall using an improved mass addition approach. Numer Heat Tran Part A-Appl 65(9):885–910
15. Alimardani M, Toyserkani E, Huissoon JP (2007) Three-dimensional numerical approach for geometrical prediction of multilayer laser solid freeform fabrication process. J Laser Appl 19(1): 14–25
16. Liu ZY, Qi H (2014) Numerical simulation of transport phenomena for a double-layer laser powder deposition of single-crystal superalloy. Metall Mater Trans A 45A(4):1903–1915
17. Kong FR, Kovacevic R (2010) Modeling of heat transfer and fluid flow in the laser multilayered cladding process. Metall Mater Trans B 41(6):1310–1320
18. Pinkerton AJ (2010) Laser direct metal deposition: theory and applications in manufacturing and maintenance. In: Advances in Laser Materials Processing: Technology, research and applications. Woodhead Publishing Ltd., Cambridge, England, pp 461–491
19. Lee PD, Quested PN, McLean M (1998) Modelling of Marangoni effects in electron beam melting. Phil Trans R Soc A 356(1739): 1027–1043

20. Xie J, Kar A, Rothenflue JA, Latham WP (1997) Temperature-dependent absorptivity and cutting capability of CO_2, Nd:YAG and chemical oxygen-iodine lasers. J Laser Appl 9(2):77–85
21. Lange DF, Hofman JT, Meijer J (2005) Optical characteristics of Nd:YAG optics and distortions at high power. In: Proceedings of the 24th International Congress on Applications of Lasers and Electro-Optics, ICALEO. Miami, FL, p 1503
22. Weisheit A, Backes G, Stromeyer R, Gasser A, Wissenbach K, Poprawe R (2001) Powder injection: the key to reconditioning and generating components using laser cladding. In: Proceedings of the International Congress on Advanced Materials and Processes, Materials Week 2001. Munich, Germany, pp 1–8
23. Mills KC (2002) Recommended values of thermophysical properties for selected commercial alloys. Woodhead Publishing Ltd., Cambridge
24. McNallan MJ, Debroy T (1991) Effect of temperature and composition on surface tension in Fe-Ni-Cr alloys containing sulfur. Metall Trans B 22(4):557–560
25. Zacharia T, David SA, Vitek JM, Debroy T (1989) Weld pool development during GTA and laser beam welding of type 304 stainless steel: part 1—theoretical analysis. Weld J 68:499S–509S
26. Carcel B, Sampedro J, Perez I, Fernandez E, Ramos JA (2010) Improved laser metal deposition (LMD) of nickel base superalloys by pyrometry process control. In: Proceedings of SPIE-The International Society for Optical Engineering. Sofia, Bulgaria, p 775123
27. Pottlacher G, Hosaeus H, Kaschnitz E, Seifter A (2002) Thermophysical properties of solid and liquid Inconel 718 Alloy. Scand J Metall 31(3):161–168
28. Su WN, Erasenthiran P, Dickens PM (2003) Investigation of fully dense laser sintering of tool steel powder using a pulsed Nd:YAG (neodymium-doped yttrium aluminium garnet) laser. Proc Inst Mech Eng Part C-J Eng Mech Eng Sci 217(1):127–138
29. Cho MH, Farson DF (2007) Simulation study of a hybrid process for the prevention of weld bead hump formation. Weld J 86(9): 253S–262S
30. Morgan R, Sutcliffe CJ, O'Neill W (2001) Experimental investigation of nanosecond pulsed Nd:YAG laser re-melted pre-placed powder beds. Rapid Prototyp J 7(3):159–172
31. Paul CP, Mishra SK, Kumar A, Kukreja LM (2013) Laser rapid manufacturing on vertical surfaces: analytical and experimental studies. Surf Coat Technol 224:18–28